Chapter 9
Electron Paramagnetic Resonance Based Spectroscopic Techniques

Pavel G. Baranov, Nikolai G. Romanov, Celso de Mello Donegá, Sergei B. Orlinskii and Jan Schmidt

Abstract This chapter addresses the use of electron paramagnetic resonance based spectroscopic techniques to study nanostructures. Particular attention is given to high frequency electron spin echo, electron-nuclear double resonance and optically detected magnetic resonance spectroscopy.

9.1 Fundamentals

Magnetic resonance methods are the basic techniques for studying spin phenomena in condensed matter and biological systems. Spin is a purely quantum-mechanical object and spin phenomena are beginning to play a crucial role in the development of devices based on nanostructures. As a result, magnetic resonance techniques have attracted increasing interest in the last few decades.

Electron paramagnetic resonance (EPR) was discovered by Zavoisky in 1944 [1, 2]. Since then, EPR based spectroscopic techniques have evolved into one of the most informative tools for investigating defects and dopants in solids. These techniques offer a uniquely sensitive probe of the chemical identity, local structural order, atomic-scale environment, and electron density distributions of defects and impurities, and have thus been used to unravel the microscopic structure of many intrinsic and impurity defects in solids [3–7].

P.G. Baranov (✉) · N.G. Romanov
Ioffe Physical-Technical Institute, St. Petersburg 194021, Russia
e-mail: pavel.baranov@mail.ioffe.ru

C. de Mello Donegá
Debye Institute for Nanomaterials Science, Utrecht University, Utrecht, The Netherlands

S.B. Orlinskii
Federal Center of Shared Facilities, Kazan State University, Kazan 420008, Russia

J. Schmidt
Huygens Laboratory, Leiden University, 2300 RA Leiden, The Netherlands

C. de Mello Donegá (ed.), *Nanoparticles*,
DOI 10.1007/978-3-662-44823-6_9

There are a variety of elegant techniques in which higher sensitivity and resolution are obtained by exciting two resonance transitions in the sample (double-resonance techniques). The great advantages of these techniques are that, in contrast to optical methods, they allow the identification of the dopants and provide information about the spatial distribution of the electronic wave function. This latter aspect is particularly attractive because it allows for a quantitative measurement of the effect of confinement on the shape and properties of the electron or hole wave function. In the following sections, we briefly address the fundamentals of three important EPR based spectroscopic techniques. The application of these techniques to nanomaterials is illustrated in Sect. 9.2.

9.1.1 Electron Spin Echo Detected Electron Paramagnetic Resonance (ESE-EPR)

In a conventional EPR experiment, the sample is placed in a microwave cavity and a magnetic field is applied to the sample such that the microwave magnetic field is normal to the static magnetic field. The ground state is normally in thermal equilibrium and so, when the microwave energy equals the separation between the magnetically split spin sublevels of the magnetic ion or defect, resonant absorption of microwave power occurs and is detected [2].

The spin echo experiment is based on the concept of an inhomogeneous broadened EPR line, which can be considered as composed of "homogeneous spin packets" (Fig. 9.1a). Microwave radiation is applied with a frequency ω_0 and polarized in the *xy*-plane. The oscillating B_1 field of this radiation can be decomposed into two counter-rotating components, one of which is rotating in the same direction as the Larmor precession of spins in magnetic field. Hence, in the rotating frame, B_1 is a stationary field, defined along *x*' [Fig. 9.1a (i)]. If the microwave field is strong, the resulting magnetic field is oriented along B_1 for every spin packet. During the presence of the microwave field the magnetization of the various spin packets, M_i, will precess around B_1 with a frequency $\omega_1 = \gamma_e B_1$, where γ_e is the giromagnetic ratio. When the duration of the microwave radiation is just enough to flip the magnetization M_i into the *xy*-plane, the pulse is defined as a $\pi/2$ pulse. Since the different spin packets have different offset frequencies ω_i', they start to dephase immediately after the pulse [Fig. 9.1a (ii)]. This process is called the Free Induction Decay (FID). From this FID, however, an echo can be generated by a second microwave pulse, applied at a time τ after the first pulse, which rotates the spins over π [Fig. 9.1a (iii)]. This π pulse is equivalent to a reflection of the dephased pattern in the x'z-plane. The original precession frequencies and the precession direction, however, remain unaltered. The result is that the spin packets refocus after the same time τ, into a macroscopic magnetic moment which produces the echo [Fig. 9.1a (iv)]. As an illustrative example, the ESE-detected EPR spectrum of Li-doped ZnO nanocrystals (NCs) is shown in Fig. 9.1b. This spectrum will be discussed in more detail below (9.2.1.1).

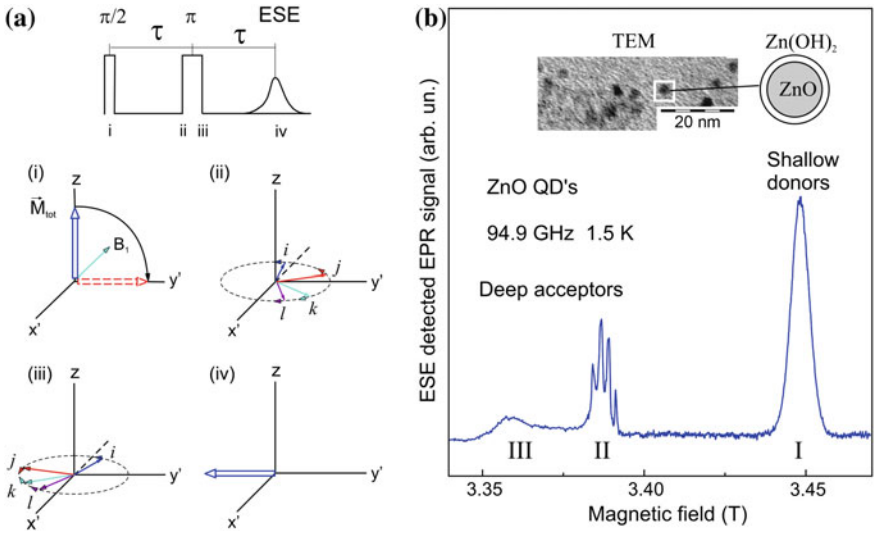

Fig. 9.1 **a** Illustration of two pulse electron spin echo (ESE) experiment: (*i*) magnetization of spin packets l,j,k, and l during the π/2 pulse, (*ii*) during the waiting time τ, (*iii*) after a pulse π, (*iv*) at the time after echo (time τ after the pulse). **b** ESE-detected EPR spectrum at 94.9 GHz and T = 1.5 K of a dry powder sample of Li-doped ZnO nanocrystals with an average diameter of 3.4 nm after 30 min UV irradiation. The inset in the top part of the figure shows a Transmission Electron Microscopy (TEM) image of the nanocrystals (*left*) and a model depicting its ZnO/Zn(OH)$_2$ core–shell structure (*right*)

9.1.2 Electron-Nuclear Double Resonance (ENDOR)

Electron-nuclear double resonance (ENDOR) is a magnetic resonance spectroscopic technique for the determination of hyperfine interactions between electrons and nuclear spins [2]. ENDOR can be considered as a method for increasing the resolution of EPR spectra and as a technique for improving NMR sensitivity for a limited number of nuclei that are located near the paramagnetic defect. There are two principal techniques. In continuous-wave ENDOR the intensity of an electron paramagnetic resonance signal, partially saturated with microwave power, is measured as radiofrequency is applied. In pulsed ENDOR the radiofrequency is applied as pulses and the EPR signal is detected as a spin-echo. In each case an enhancement of the EPR signal is observed when the radiofrequency is in resonance with the coupled nuclei and the nuclear-spin transitions are detected as changes in the EPR signal.

9.1.3 Optically Detected Magnetic Resonance (ODMR)

In optically detected magnetic resonance (ODMR), the population redistribution among magnetic sub-states, in passage through magnetic resonance in the ground or

excited state of a paramagnetic centre, produces a change in some aspect of either emitted or absorbed light associated with the centre [3]. The scaling up of the EPR detection from the microwave to the optical region renders these optical EPR methods extremely sensitive.

The resonance conditions are created in the same way as in conventional EPR experiment but instead of direct measurements of microwave resonant absorption, microwave induced changes in optical processes (viz., luminescence intensity or polarization, magnetic circular dichroism in optical absorption) are detected. Optical absorption or emission transitions are in some degree dependent on the population of the magnetic (spin) sublevels of the system under investigation. Therefore, magnetic resonance, by changing the populations of the spin sublevels, can induce changes in optical absorption and/or emission transitions (intensity or polarization). ODMR is thus a kind of a "trigger" detection since absorption of a microwave quantum results in additional emission (or absorption) of an optical photon with several orders of magnitude higher energy. This results in a huge increase in sensitivity, making it possible to detect a very small number of spins, down to the single spin level. In addition, ODMR provides spatial selectivity since, opposite to conventional EPR, magnetic resonance is measured only in optically active regions of the sample. Another selectivity channel is provided by appropriate selection of an optical spectral range in which ODMR is measured. Due to these advantages ODMR can be effectively applied for a study of nanostructures (see [6, 7] and references therein).

9.2 Applications to Nanomaterials

Understanding the structure and constituents of defects in nanostructures is crucially important since defects and impurities can greatly affect the properties of nanomaterials. EPR spectroscopy has been widely applied to characterize paramagnetic ions (*e.g.*, Mn^{2+}) in nanocrystals (NCs), as it allows dopants at the surface to be distinguished from those in the interior of the NC [8]. During the last two decades high-frequency (high-field) EPR and in particular pulse EPR and pulse ENDOR spectroscopy developed to a new fast advancing field in magnetic resonance spectroscopy [4]. These techniques were shown to be excellent tools for the investigation of the electronic properties of semiconductor NCs, allowing the interaction between the exciton and paramagnetic impurities to be probed, as well as the observation of photoexcited carriers bound to impurities (i.e., donor and acceptor centers) [5, 6]. In combination with optical excitation, EPR (photo-EPR) can also yield information regarding optical transitions and energy-level positions, thus providing a bridge between optical and magnetic resonance spectroscopy. Direct measurements of EPR and ENDOR in nanostructures are often difficult because of the small total number of spins, therefore ODMR is much better suited for such systems [6, 7]. Electron paramagnetic resonance based spectroscopic techniques have been successfully applied to a variety of nanocrystalline materials

(e.g., colloidal InP and CdTe NCs [7], silver halide NCs embedded in an alkali halide matrix [9], free-standing diamond NCs [10–12], etc.). One selected case (viz., ZnO nanocrystals) will be addressed below as an illustrative example.

9.2.1 ZnO Nanocrystals

ZnO offers a unique combination of high band gap energies, cohesion and exciton stability. ZnO quantum dots (QDs) are particularly attractive since the confinement of the electronic wave function allows the optical and electronic properties to be tuned. Doped ZnO nanocrystals (NCs), which can be easily processed at temperatures much lower than those for bulk ZnO crystals, are of particular interest due to their potential use in light-emitting and photovoltaic devices. In the next sections we will discuss experimental results obtained on powder samples of free-standing hydroxyl-capped ZnO NCs with average diameter ranging from 2.2 to 6 nm. These NCs were prepared by using a colloidal synthesis method based on the hydrolysis of Zn^{2+} ions in absolute alcohols [5]. A transmission electron microscopy (TEM) image of a representative sample and a model of the $ZnO/Zn(OH)_2$ core–shell structure are shown in Fig. 9.1b above.

9.2.1.1 The Identification of the Binding Core of Shallow Donors and Deep Acceptors in ZnO Nanocrystals by EPR and ENDOR

Figure 9.1b shows the ESE-detected EPR spectrum of a dry powder sample of Li-doped ZnO NCs with an average diameter of 3.4 nm. The EPR spectrum appears after illumination with above-band-gap light during 30 min at 1.6 K and persists at low temperature after switching off the light. The signal I is assigned to a shallow donor. Its average g-value $g_{av} = 1.9666$ differs somewhat from the $g_{\|} = 1.9569$ and $g_{\perp} = 1.9552$ values obtained for the interstitial-hydrogen donor in a single crystal of ZnO. The EPR signals labelled (II) and (III) are assigned to deep acceptors. A prerequisite for the observation of the EPR signal of the unpaired spin of shallow donors at liquid-helium temperatures is that the ZnO NCs are first illuminated with above-band-gap light. This observation shows that there must be deep acceptors present in the nanocrystals that capture the thermally excited donor electrons at room temperature. Apparently these electrons remain frozen at the acceptor when the material is cooled in the dark to low temperature. The above-band-gap light transfers the electron from the acceptor to the donor and makes both sites paramagnetic. The spectrum disappears when the temperature is increased above 200 K.

We will focus on the EPR signal I assigned to the shallow donor. The signal is ascribed to a donor because g_{av} is smaller than the g-value of a free electron.The shallow character becomes clear from the dependence of g_{av} on the size of the NCs, as will be discussed in Sect. 9.2.1.2. This shift towards the free-electron g_e-value with decrease of the NC size is caused by the confinement of the hydrogen-like

1s-type wave function of shallow donors when their Bohr radius becomes comparable to the size of the NC.

The EPR spectrum in Fig. 9.1b does not provide information on the chemical nature of the donor since no resolved hyperfine (HF) structure is observed, as is the case for the In and Ga shallow donors in ZnO bulk crystals. To identify the binding core, ENDOR experiments were performed. Figure 9.2 shows the ESE-detected ENDOR transitions observed on the EPR signal I (Fig. 9.1) of the shallow donor in Li-doped ZnO NCs with radius of 1.7 nm. Similar experiments were carried out on the EPR signal of the shallow donors in Na-doped ZnO NCs with radius of 1.7 nm and in Al-doped ZnO NCs with radius of 2.5 nm (Fig. 9.3). The pulse sequence for the ENDOR experiments is shown in the top panels of Figs. 9.2 and 9.3. In the pulsed ENDOR experiment, a Mims-type pulse sequence was used. It consists of three $\pi/2$ microwave pulses with separation τ and T between the first and the second and the second and the third pulse, respectively, and creates a stimulated echo at a time τ after the last pulse. A radio-frequency (RF) pulse, which is applied between the second and the third microwave pulse, induces a change in the intensity of the stimulated echo when this RF pulse is resonant with a nuclear magnetic resonance (NMR) transition. The ENDOR spectra are obtained by monitoring the stimulated echo intensity as a function of the frequency of the RF field.

To understand these results we consider the isotropic HF interaction or Fermi contact term a_i which reflects the spin density of the donor electron wave function at the site of the nucleus (r_i)

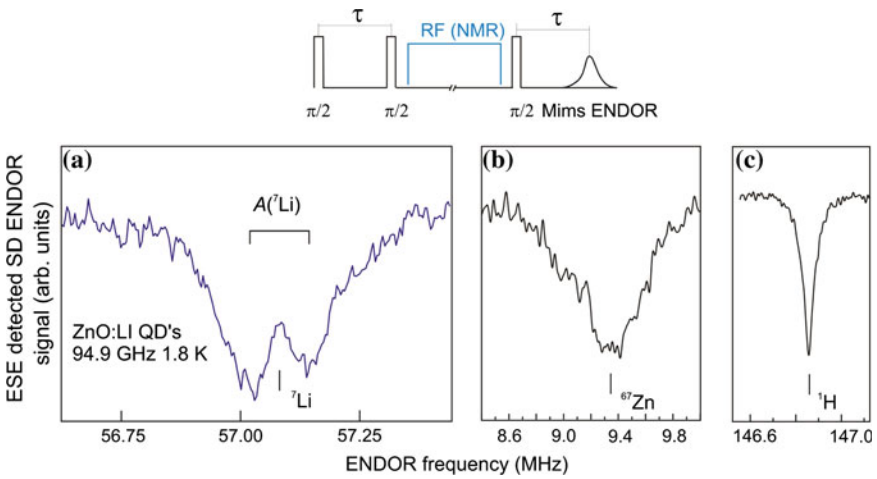

Fig. 9.2 ESE-detected ENDOR transitions of the ^{7}Li (**a**), ^{67}Zn (**b**), and ^{1}H (**c**) nuclear spins as observed in the EPR signal I (see Fig. 9.1) of the shallow donors in Li-doped ZnO nanocrystals with an average size of 3.4 nm. The Zeeman frequency of ^{7}Li, ^{67}Zn, and ^{1}H are marked by bars. The pulse sequence for the ENDOR experiments is shown in the top panel

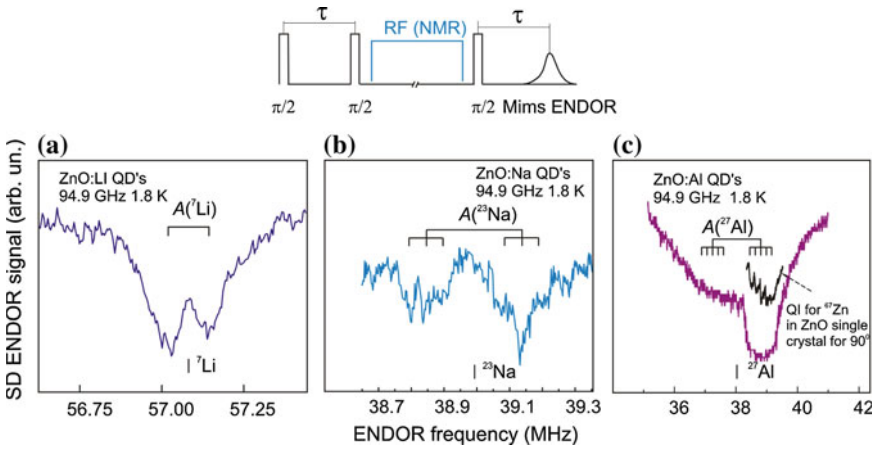

Fig. 9.3 ESE-detected ENDOR transitions as observed in the EPR signal I (see Fig. 9.1b) of the shallow donors in Li-doped ZnO NCs (**a**) and Na-doped ZnO NCs (**b**) with an average size of 3.4 nm, and Al-doped ZnO NCs with an average size of 5 nm **c** recorded at 94.9 GHz and T = 1.8 K. The ENDOR transitions are symmetrically placed around the Zeeman frequency of ^{7}Li, ^{23}Na, and ^{27}Al, respectively (marked by bars). The pulse sequence for the ENDOR experiments is shown in the top panel

$$a_i = (8\pi/3) g_e \beta_e g_{ni} \beta_n |\Psi(r_i)|^2 \tag{9.1}$$

where g_e is the electronic g-factor, β_e is the electronic Bohr magneton, g_{ni} is the g-factor of nucleus i, and β_n is the nuclear magneton. The related ENDOR transition frequencies are

$$\nu_{ENDOR} = h^{-1} |g_{ni} \beta_n B_0 \pm a_i/2| \tag{9.2}$$

Equation (9.2) predicts that each nucleus i gives rise to two ENDOR transitions symmetrically placed around its nuclear Zeeman frequency $g_{ni}\ \beta_n B_0/h$ when the quadrupole interaction is neglected and when $a_i < g_{ni}\ \beta_n B_0$. The ENDOR signals in Figs. 9.2 and 9.3 are symmetrically placed around the Zeeman frequencies of ^{7}Li, ^{23}Na, and ^{27}Al, respectively, which gives an unambiguous identification of the shallow donor core as Li-, Na-, or Al-related centres. Moreover, the observed HF splitting gives direct information about the density of unpaired electron spin of the shallow donor at the Li, Na and Al nuclei since the isotropic HF splitting is proportional to the wavefunction density. Further, it is seen in Fig. 9.2b that symmetrically around the Zeeman frequency of ^{67}Zn (I = 5/2, abundance 4.1 %) at 9.2 MHz a broad, unresolved set of ENDOR lines of ^{67}Zn spins is present. From the multitude of lines it is clear that we are indeed dealing with a delocalised electron of a shallow donor that interacts with a large number (tens) of ^{67}Zn nuclei [5]. The box-like form of the ENDOR spectra in Figs. 9.3b, c is explained by the quadrupole interaction of the ^{23}Na and ^{27}Al nuclei, which gives rise to three and five unresolved

ENDOR lines, respectively. In addition, ENDOR lines exactly at the Zeeman frequency of ^{1}H were found in these ZnO NCs (Fig. 9.2c). From the width of the line a ^{1}H HF interaction smaller than 60 kHz can be deduced. This should be compared to the hyperfine splitting of 1.4 MHz between the two ENDOR lines previously observed on the hydrogen-related shallow donor in bulk ZnO crystals [5]. This shows that the observed ENDOR lines originate in the hydrogen atoms present in the $Zn(OH)_2$ capping layer where the density of the electronic wave function is very small.

The EPR signal (II) in Fig. 9.1 exhibits a nearly isotropic hyperfine splitting that suggests a hyperfine interaction with a nucleus of spin $I = 3/2$ with an almost 100 % abundance. This observation favours a Na-related centre and indeed the ENDOR spectrum confirms this assignment. The conclusion that this deep Na-related centre is located close to or at the $ZnO/Zn(OH)_2$ interface is drawn from the observation that the ENDOR signals of both the ^{23}Na ($I = 3/2$) and the ^{1}H ($I = 1/2$) nuclei can be observed in the EPR signal II. The line width of 1.0 MHz is about 8 times larger than that of the ^{1}H ENDOR signals observed in the ESE-detected EPR signal of the Li-related donor (Fig. 9.2c). This shows that the density of the electronic wave function of the Na-related acceptor is relatively large in the $Zn(OH)_2$ capping layer. The main contribution to the EPR signal III (Fig. 9.1) comes from deep zinc vacancy acceptors. Zinc vacancies may be introduced during the growth of the NCs. This conclusion is supported by the results of ODMR measurements (see 9.2.1.4 below).

Figure 9.4a shows the ^{67}Zn ENDOR spectra in ZnO NCs of various sizes. The remarkable observation in Fig. 9.4 is that upon reduction of the size of the ZnO NCs the distribution of ENDOR lines broadens and a dip develops around the Zeeman frequency of the ^{67}Zn nuclear spins. The dip becomes more prominent and broader

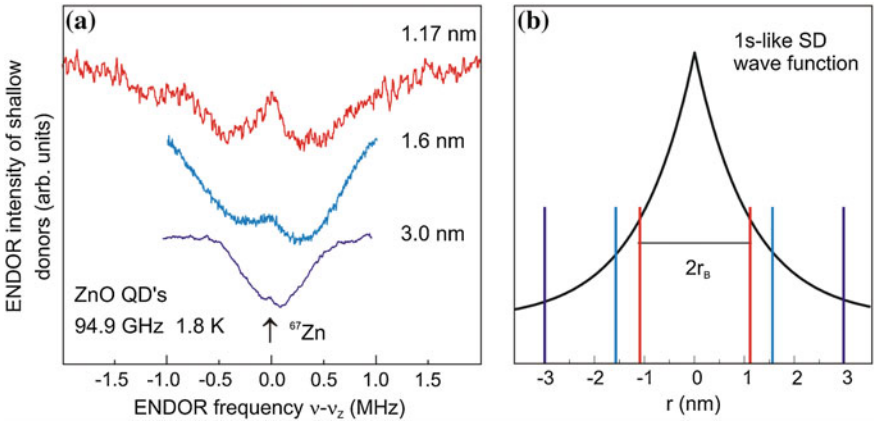

Fig. 9.4 **a** ENDOR spectra of the ^{67}Zn nuclear spins in ZnO NCs with radii of 1.17, 1.6 and 3.0 nm recorded at 94.9 GHz and T = 1.8 K. Each spectrum consists of many unresolved lines placed symmetrically around the Zeeman frequency (*marked by arrows*) of the ^{67}Zn nuclear spins. **b** Schematic representation of the 1 s-like wave function density for shallow donors

when the radius of the ZnO core is reduced from 3.0 to 1.6–1.17 nm. The broadening of the ENDOR signal indicates that the maximum density of the electronic wave function increases when reducing the size of the NCs. The disappearance of the ENDOR signals close to the ^{67}Zn Zeeman frequency shows that remote shells are missing in the small NCs as illustrated by bars in Fig. 9.4b.

9.2.1.2 Probing the Wave Function of Shallow Donors in ZnO Nanocrystals and Confinement Effects

The ENDOR studies allow the effects of confinement on the spatially extended wave function of the shallow donor to be probed by measuring the isotropic hyperfine (HF) interaction, which reflects the spin density at the site of the nucleus, and by varying the particle size in the quantum-size regime [5]. The ^{7}Li ENDOR signals are excellently suited for this purpose. Figure 9.5 shows the values of the isotropic HF interaction A of the ^{7}Li nuclear spin (a) and the wavefunction density of the shallow Li-related donor at the interface of the ZnO core (b) as a function of the NC size. The error bars in the values of A are estimated from the noise in the ENDOR spectra and the size distribution of the particles derived from TEM and powder X-ray diffraction measurements. The dashed line is a fit to the measured

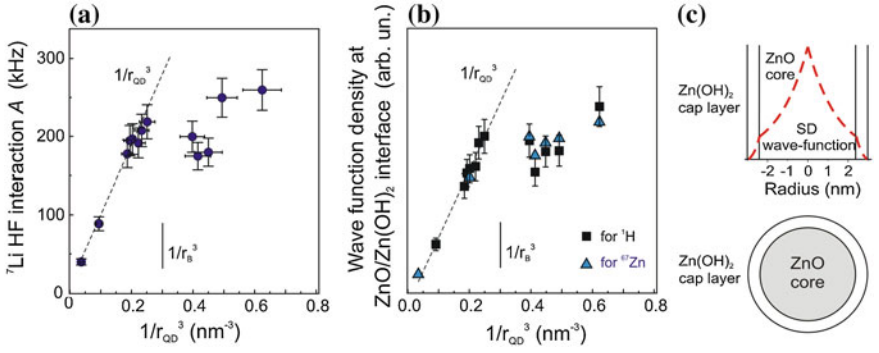

Fig. 9.5 **a** Isotropic hyperfine interaction A of the ^{7}Li nuclear spin of the shallow Li-related donors in ZnO NCs with radii between 3.0 and 1.1 nm. The *black circles* indicate the hyperfine splitting as observed in the ENDOR spectra at T = 1.2 K. The error bar in the values of A_{iso} is estimated from the noise in the ENDOR spectra. The variation in the size of the NCs is derived from Transmission Electron Microscopy and powder X-Ray Diffraction measurements. The *dashed line* is a fit to the measured values of A for NCs with radii between 3.0 and 1.5 nm using the function R^{-3}. **b** Variation of the wave function density at the interface of the ZnO core and the $Zn(OH)_2$ capping layer for the NCs as calculated from the dip in ENDOR of the ^{7}Li nuclear spin (*core side, squares*) and from the width of the ENDOR line of the ^{1}H nuclear spins in the $Zn(OH)_2$ capping layer (*triangles*). The dashed line is a fit to the measured values for NCs with radii between 3.0 and 1.5 nm using the function $*R^{-3}$. **c** Sketch of the wave function of the shallow donor in a ZnO quantum dot capped by a $Zn(OH)_2$ layer and a model of the ZnO/$Zn(OH)_2$ core–shell structure

values for NCs with radii between 3.0 and 1.5 nm using a function proportional to r^{-3}. The experimental results follow quite closely this dependence down to R = 1.5 nm, a value which is equal to the Bohr radius of the shallow donor, while for smaller radii a considerable deviation is observed. A sketch of the hydrogen-like wave function in ZnO quantum dots together with a model of the ZnO/$Zn(OH)_2$ core–shell structure are shown in Fig. 9.5c. It is thus clear that the model based on the effective-mass approximation does not yield an appropriate description of the electronic wave function when the NC radius is reduced below the Bohr radius. We suggest that molecular, cluster-type calculations should be carried out to describe the observed behaviour.

The shallow character of the Li-related donor is also visible in the dependence of the g-factor on the size of the ZnO NC (Fig. 9.6). The shift of the g-factor towards the free-electron value upon size reduction is caused by the spatial confinement of the shallow donors when the NC size becomes comparable to the Bohr radius of their hydrogen-like 1s-type wave functions. The effect is explained by the reduction of the admixture of valence-band states and higher-lying conduction bands into the

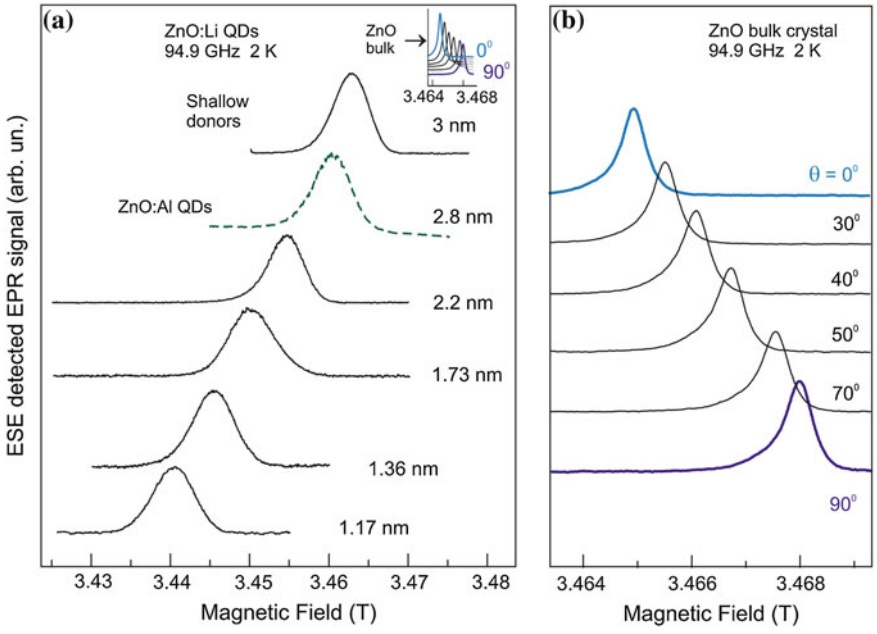

Fig. 9.6 **a** ESE-detected EPR spectra of shallow donors (SDs) in ZnO NCs with radii of 1.17, 1.36, 1.73, 2.2, 2.8 and 3 nm recorded at 94.9 GHz and T = 2 K. The solid lines are the ESE-detected EPR spectra of ZnO:Li NCs. The *dashed line* is the ESE-detected EPR spectra of ZnO:Al NCs. The inset shows the angular dependence of the ESE-detected EPR spectra of H-related SDs in ZnO bulk crystal presented on the same magnetic-field scale. This dependence in larger magnetic-field scale is presented in **b**, θ is the angle between the magnetic field direction and the c-axis of ZnO crystal

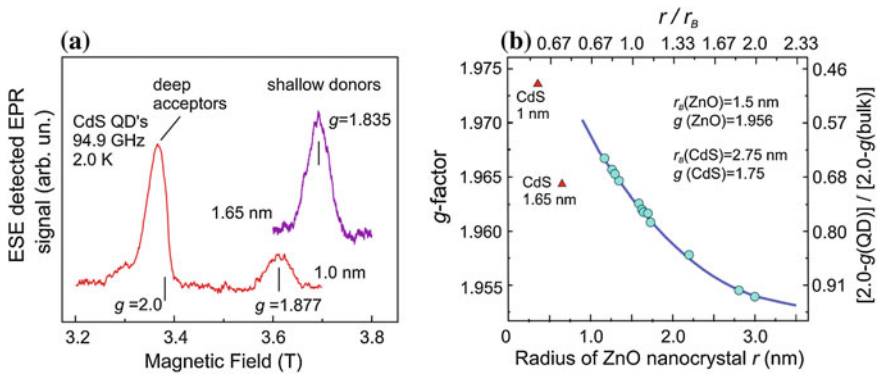

Fig. 9.7 **a** ESE-detected EPR spectra of SDs in CdS NCs with radii of 1.65 and 1.0 nm recorded at 94.9 GHz and T = 2.0 K. **b** Dependence of the *g*-factor of the shallow donor on the size of the ZnO NC. The upper scale gives the NC radius normalized to the Bohr radius r_B of the SD in the related bulk semiconductor. The right scale gives a *g*-factor shift of the SD in NC from $g = 2.0$ normalized to that for the bulk material. The filled tringles indicate the *g*-factor shift in CdS NCs on the normalized scale

lowest conduction band by the increase of the band-gap energy and the energy of higher-lying conduction bands upon the reduction of the NC size. For comparison, the anisotropic EPR spectra of the shallow hydrogen-related donors in a bulk ZnO crystal are presented in the top of Fig. 9.6 for several orientations of the magnetic field with respect to the *c*-axis. A line width close to that in ZnO NCs is obtained by averaging of the signal, under the assumption that the ZnO NCs are randomly oriented. A similar effect is observed in free-standing polyphosphate-capped CdS NCs with diameters of 2 and 3.3 nm (Fig. 9.7). The influence of the confinement effect on the *g*-factor of these shallow donors is visible in Fig. 9.7. The dependence of the *g*-factor of the shallow Li-related donor on the size of the ZnO NCs is also displayed for comparison. It is clear that the data on ZnO and CdS NCs cannot be fitted with the same dependence. It remains for theoreticians to explain these different behaviours.

9.2.1.3 Dynamic Nuclear Polarization of Nuclear Spins in ZnO Nanocrystals

Dynamic nuclear polarization (DNP) is a general method of enhancing by several orders the polarization of a nuclear spin system in interaction with an electron spin system by saturation of a suitable resonance of the combined system. The nuclear spins in a QD become polarized by the Overhauser effect when the EPR transitions of the shallow donor are excited by microwave irradiation [5]. These polarized nuclear spins create an internal magnetic field and, as a result, the resonance line of the electron spins, subjected to the microwave irradiation, shifts to a lower external field value resulting in a hole and an antihole in the inhomogeneously broadened

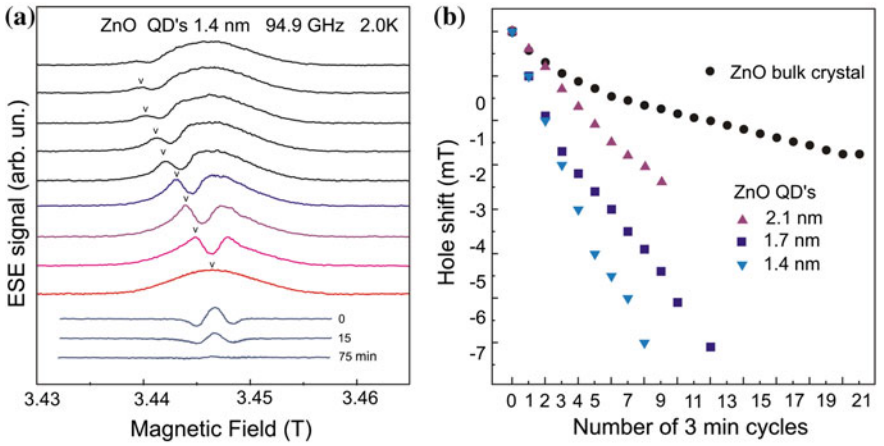

Fig. 9.8 **a** Shift of the hole in the EPR transition of the shallow Li donor in ZnO NCs with radius of 1.4 nm induced by cw microwave irradiation at 94.9 GHz and T = 2 K. The *lowest* EPR line is recorded without pre-irradiation. The second recording from the *bottom* is obtained after cw microwave irradiation during 3 min at the centre of the unperturbed line. The next curves are observed after cw microwave irradiation during 3 min at the maximum of the antihole of the previous recording. Finally, the antihole stabilizes at a position shifted by 7 mT with respect to the original position. The spectrum labelled by (0) represents the difference between two *upper curves*. Curves (15) and (75) are recorded 15 and 75 min after the pre-irradiation, respectively (the upper unperturbed line was subtracted from each spectrum). **b** Shift of the hole and the antihole versus the number of 3-min cycles of cw microwave irradiation in the 94.9 GHz EPR line of shallow Li-related donors in ZnO NCs with radii of 1.4, 1.7 and 2.1 nm, and that of the shallow H donors in a ZnO single crystal. $T = 2$ K

EPR line. Figure 9.8a shows the shift of the hole in the EPR transition of the shallow Li donor in ZnO NCs with a radius of 1.4 nm induced by exposing the samples to subsequent pre-irradiations with continuous wave (cw) microwaves. It is seen that slowly the hole and the "antihole" decrease and the EPR spectrum recovers its initial unperturbed form. The maximum shift of the antihole depends on the NC size (see Fig. 9.8b).

The creation of the hole and antihole in the EPR line of shallow donors in ZnO NCs is caused by dynamic nuclear polarization (DNP) of the ^{67}Zn ($I = 5/2$) nuclear spins and of the ^{1}H ($I = 1/2$) nuclear spins in the $Zn(OH)_2$ capping layer. Since the line width of the Li donor in a sample of randomly oriented ZnO NCs depends to a large extent on the anisotropy of the g-tensor, the hole in the line corresponds to electron spins of Li donors in ZnO NCs with a given orientation of their hexagonal crystal axis with respect to the external magnetic field. The striking result is that the intensity of the induced hole depends on the orientation of dry powder sample. The hole was observed to disappear after a rotation by 90° and to reappear at the same position after the reverse rotation or a rotation by 180°. This shows that one can select a particular orientation in a sample of randomly oriented NCs.

9.2.1.4 ODMR via Tunnelling Afterglow in ZnO Nanocrystals

In this subsection, we will consider one of the ODMR techniques which is based on EPR detection via tunnelling afterglow. This afterglow can be observed after X-ray or UV irradiation and in some cases persists for a long time after the irradiation. This technique was first applied for ionic crystals and proved to be very useful to study colloidal ZnO NCs.

The tunnelling afterglow is determined by the recombination of electron and hole centres that were created during irradiation. The recombination is forbidden for electrons and holes with parallel spins. Therefore, in the magnetic field at a low temperature, when all spins tend to orient along the field as a result of the Boltzmann polarization, the afterglow intensity decreases. The magnetic quenching of the afterglow can be described by the relationship

$$I(B,t) = I_0(t)(1 - P_e P_h) \tag{9.3}$$

where I_0(t) is the afterglow intensity in zero field, which decreases slowly with time according to a hyperbolic law, and P_e and P_h are the spin polarizations of the electron and hole centres, respectively. For centres with the electron spin $S = 1/2$, the spin polarization can be calculated from

$$P_{e,h} = \tanh(g_{e,h}\mu_B B/2\kappa T) \tag{9.4}$$

where $g_\mathrm{e,h}$ is the electron g factor of an electron (e) or a hole (h) centres and μ_B is the Bohr magneton. The spin polarization $P_\mathrm{e,h}$ increases with an increase in the magnetic field and with a decrease in the temperature and tends to zero in high magnetic fields. At saturation of the EPR transition $P_{e,h}$ tends to zero, since the populations of the levels with spin up and down become equal, and a resonance increase in the emission intensity appears. For a distant pair of an electron and a hole centres the overlap of their wave functions is weak and the exchange interaction can be neglected. Therefore the ODMR spectrum consists of the individual EPR signals of the electron centre and the hole centre. The sensitivity and resolution of the afterglow-detected ODMR can be considerably increased with an increase in the ODMR operating frequency, as shown in Fig. 9.9a.

The photoluminescence (PL) and afterglow spectra of ZnO NCs are shown in Fig. 9.9b. Two emission bands are observed in the PL spectra: a relatively weak and narrow UV exciton emission and a much stronger and broader emission band in the green part of the visible spectrum, which is ascribed to recombination of a shallowly trapped electron with a deeply trapped hole [13]. In contrast, in the afterglow spectrum only the broad emission band is observed. Long-lasting afterglow (up to 3 h after switching off the UV excitation) was observed in Li-, Na- and Al-doped ZnO NCs. The afterglow intensity did not depend on temperature in the range 2–10 K, and was therefore assigned to tunnelling recombination of donor and acceptor centres that had been created by a short term UV excitation.

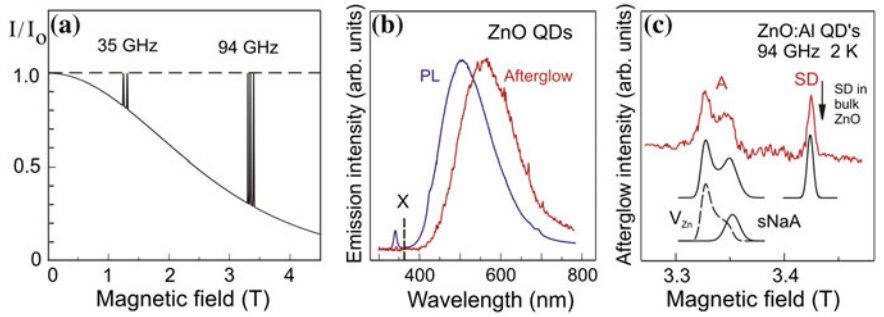

Fig. 9.9 **a** Dependence of the tunnelling afterglow intensity on the magnetic field at T = 2 K for two recombination centres with S = 1/2 and different *g*-factors according to the calculations from Eqs. (9.3) and (9.4), with the ODMR signals of these centres at frequencies of 35 and 94 GHz that correspond to a complete saturation of EPR transitions. **b** Photoluminescence (PL) and afterglow spectra of a diluted suspension of colloidal ZnO NCs (3.5 nm diameter) in ethanol. The temperature was maintained at 2 K in both cases. The afterglow spectrum was recorded 1 h after switching off UV irradiation. The *dashed line* marked with X indicates the position of the exciton luminescence line for bulk ZnO. **c** ODMR spectrum recorded in the W band (94 GHz) from the afterglow intensity for the same NCs at a temperature of 2 K. The arrow indicates the position of the EPR line of shallow donors in the bulk ZnO crystals for the magnetic field orientation perpendicular to the c crystal axis. The EPR spectra simulated for shallow donors and deep acceptors of two types, i.e., the zinc vacancies (V_{Zn}) and surface Na-related acceptors (sNaA), are shown at the *bottom*

The ODMR spectrum of ZnO:Al NCs recorded at 94 GHz on the afterglow intensity is shown in Fig. 9.9c. Shallow donors and two types of acceptors were resolved. The acceptors were identified as the zinc vacancy acceptors and the surface Na acceptors since the shape of the experimental spectrum is in good agreement with the spectrum simulated with the known parameters of these centres.

ODMR detected via afterglow of UV irradiated ZnO NCs can be used to estimate the NC size from the experimental values of the shallow donor *g*-factor and the magnitude of *g*-factor shown in Fig. 9.7b. It should be pointed out that the higher sensitivity of ODMR allows its application in the characterization of ZnO NCs dispersed in transparent media (such as polymers and frozen solvents), which cannot be studied by conventional EPR and ESE. This is an important advantage, since these systems are more relevant for a number of practical applications.

9.3 Outlook

EPR based spectroscopic techniques have developed into of the most powerful tools to investigate dopants and defects in condensed matter, and also provide essential information on the fate of photoexcited charge carriers in solids. These techniques have greatly contributed towards a deeper understanding of spin phenomena in

dopants and defects in nanostructures, which has important consequences for a number of potential applications in electronic, photovoltaic and spintronic devices.

In this chapter, the fundamentals of three important EPR based spectroscopic techniques were addressed. Further, the application of these techniques to nanomaterials was discussed, using ZnO nanocrystals as an illustrative example. EPR and ENDOR experiments on ZnO nanocrystals having ZnO/$(ZnOH)_2$ core/shell structures reveal the presence of shallow donors related to interstitial lithium and sodium atoms, and substitutional aluminium, in ZnO:Li, ZnO:Na and ZnO:Al nanocrystals, respectively. The shallow character of the shallow donor wave function is evidenced by the multitude of ^{67}Zn ENDOR lines and further by the hyperfine interaction s with the ^{7}Li, ^{23}Na and ^{27}Al nuclei that are much smaller than for atomic lithium, sodium and aluminium. The results show that one can monitor the change of the electronic wave function of a shallow donor in a ZnO nanocrystal when entering the regime of quantum confinement by using the nuclear spins in the semiconductor nanocrystals as probes. The ENDOR measurements show that the model based on the effective-mass approximation does not yield an appropriate description of the electronic wave function when the radius of the nanocrystal is reduced below the Bohr radius. The influence of confinement effects on the value of the *g*-factor of shallow donors has been observed for both ZnO and CdS nanocrystals. Long lasting tunnelling afterglow was found in ZnO nanocrystals and shallow donors centres and deep acceptors were identified by ODMR.

A future prospect for the technique seems to be connected with its application for the study and characterization of a wide range of nanostructures, including quantum dots doped with magnetic ions, self-organized nanostructured systems such as semiconductor nanocrystals embedded in glass and ionic crystal matrices, diamond nanocrystals, and organic-nanoinorganic photovoltaic structures, which aim to integrate the inexpensive processing properties of polymers with the superior optical, electrical, and carrier transport properties of nanoscale inorganic semiconductors.

9.4 Exercises

1. How can EPR spectroscopy be used to assess the average size of an ensemble of ZnO nanocrystals?
2. How does the size distribution of nanocrystals affect the width of the EPR line of shallow donors?
3. What are advantages of high frequency EPR in investigations of nanocrystals?
4. Estimate the shift of the EPR line of shallow donors in ZnO nanocrystals in X-band (9.3 GHz) and W-band (94 GHz) for nanocrystal radii changing from 2 to 3 nm.

Acknowledgments The work described in this chapter has been supported by the Russian Science Foundation under Agreement #14-12-00859.

References

1. Zavoisky, E.: The paramagnetic absorption of a solution in parallel fields. J. Phys. **8**, 377–380 (1944)
2. Abragam, A., Bleaney, B.: Electron Paramagnetic Resonance of Transition Ions. Oxford University Press, London (1970)
3. Geschwind, S.: Optical techniques in EPR in solids. In: Geshwind, S. (ed.) Electron Paramagnetic Resonance, pp. 353–425. New York, Plenum (1972)
4. Schweiger, A., Jeschke, G.: Principles of Pulse Electron Paramagnetic Resonance. Oxford University Press, London (2001)
5. Baranov, P.G., Orlinskii, S.B., Donega, C. d. M., Schmidt, J.: High-Frequency EPR and ENDOR spectroscopy on semiconductor quantum dots. Appl. Magn. Reson. **39**, 151–183 (2010) (and references therein)
6. Baranov, P.G., Romanov, N.G.: Magnetic resonance in micro- and nanostructures. Appl. Magn. Reson. **21**, 165–193 (2001). (and references therein)
7. Lifshitz, E., Fradkin, L., Glozman, A., Langof, L.: Optically detected magnetic resonance studies of colloidal semiconductor nanocrystals. Annu. Rev. Phys. Chem. **55**, 509–557 (2004). (and references therein)
8. Synthesis and properties of colloidal heteronanocrystals: Donega, C. d. M. Chem. Soc. Rev. **40**, 1512–1546 (2011)
9. Baranov, P.G., Romanov, N.G., Poluektov, O.G., Schmidt, J.: Self-Trapped excitons in ionic-covalent silver halide crystals and nanostructures: High-frequency EPR, ESE, ENDOR and ODMR studies. Appl. Magn. Reson. **39**, 453–486 (2010)
10. Fang, X.W., Mao, J.D., Levin, E.M., Schmidt-Rohr, K.: Non-aromatic core-shell structure of nanodiamond from solid-state NMR spectroscopy. J. Am. Chem. Soc. **131**, 1426–1435 (2009)
11. Bradac, C., Gaebel, T., Naidoo, N., Sellars, M.J., Twamley, J., Brown, L.J., Barnard, A.S., Plakhotnik, T., Zvyagin, A.V., Rabeau, J.R.: Observation and control of blinking nitrogen-vacancy centres in discrete nanodiamonds. Nat. Nanotechnol. **5**, 345–349 (2010)
12. Baranov, P.G., Soltamova, A.A., Tolmachev, D.O., Romanov, N.G., Babunts, R.A., Shakhov, F.M., Kidalov, S.V., Vul', A.Ya., Mamin, G.V., Orlinskii, S.B., Silkin, N.I.: Enormously high concentrations of fluorescent nitrogen-vacancy centers fabricated by sintering of detonation nanodiamonds. Small **7**, 1533–1537 (2011)
13. Orlinskii, S.B., Blok, H., Schmidt, J., Baranov, P.G., de Mello Donegá, C., Meijerink, A.: Donor-acceptor pairs in the confined structure of ZnO nanocrystals. Phys. Rev. B **74**, 045204 (2006)